


Article

Electrocatalytic Hydrogen Evolution Reaction of Cobalt Triaryl Corrole Bearing Nitro Group

Jie Zeng ¹, Xu-You Cao ¹, Shi-Yin Xu ¹, Yi-Feng Qiu ¹, Jun-Ying Chen ^{1,*}, Li-Ping Si ^{1,2} and Hai-Yang Liu ^{1,*} 

¹ Guangdong Provincial Key Laboratory of Fuel Cell Technology, School of Chemistry and Chemical Engineering, South China University of Technology, Guangzhou 510641, China; 202120123638@mail.scut.edu.cn (J.Z.); 202220122631@mail.scut.edu.cn (X.-Y.C.); xsy870260363@163.com (S.-Y.X.); 202221025069@mail.scut.edu.cn (Y.-F.Q.); lipingsi@fosu.edu.cn (L.-P.S.)
² School of Materials Science and Energy, Foshan University, Foshan 528000, China
* Correspondence: cejychen@scut.edu.cn (J.-Y.C.); chhyliu@scut.edu.cn (H.-Y.L.)

Abstract: The use of non-precious metals for electrocatalytic hydrogen reaction (HER) is particularly important for energy conservation and environmental protection. In this work, three new cobalt corroles containing *o*-, *m*-, and *p*-nitrobenzyl (**1**, **2**, **3**) at the *meso* 10-position of the corrole macrocycle were synthesized, and their electrocatalytic hydrogen evolution reaction in organic and neutral aqueous systems was also investigated. The results show that these three cobalt corroles have significant catalytic HER activity in both systems, and the catalytic efficiency follows **1** > **3** > **2**, which indicates that the position of the nitro group can affect the catalytic property of the complexes. In the organic phase, when using trifluoroacetic acid or *p*-toluenesulfonic acid as the proton source, the electrocatalytic HER may undergo an EECC (E: electron transfer, C: proton coupling) pathway. In a neutral aqueous system, the HER turnover frequency value of **1** is up to 137.4 h⁻¹ at 938 mV overpotential.

Keywords: corrole; cobalt; electrocatalysis; hydrogen evolution; nitro group



Citation: Zeng, J.; Cao, X.-Y.; Xu, S.-Y.; Qiu, Y.-F.; Chen, J.-Y.; Si, L.-P.; Liu, H.-Y. Electrocatalytic Hydrogen Evolution Reaction of Cobalt Triaryl Corrole Bearing Nitro Group. *Catalysts* **2024**, *14*, 454. <https://doi.org/10.3390/catal14070454>

Academic Editor: David Sebastián

Received: 11 June 2024

Revised: 8 July 2024

Accepted: 12 July 2024

Published: 15 July 2024



Copyright: © 2024 by the authors. Licensee MDPI, Basel, Switzerland. This article is an open access article distributed under the terms and conditions of the Creative Commons Attribution (CC BY) license (<https://creativecommons.org/licenses/by/4.0/>).

1. Introduction

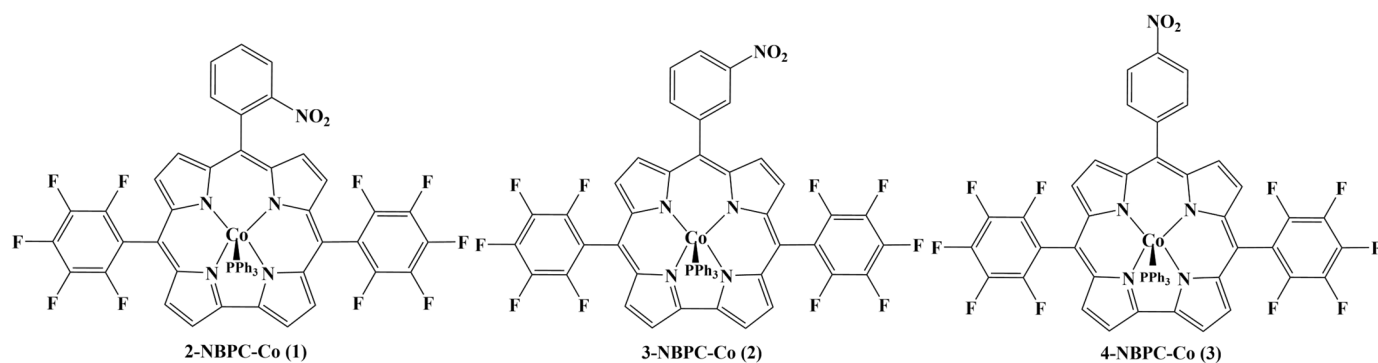
Due to the low utilization efficiency of nonrenewable traditional fossil fuels such as coal, oil, and natural gas, the continuous consumption of fossil fuels will lead to resource shortage or even depletion [1,2]. At the same time, the use of fossil fuels faces issues such as the emission of toxic and harmful particulate matter, carbon dioxide, and sulfides, which will lead to environmental pollution and the exacerbation of global warming [3–5]. Therefore, it is urgent to find clean, economical, and renewable energy alternatives [6].

Green energy such as solar, wind, hydro, geothermal, ocean thermal, and biomass are the best choices to replace fossil fuels [7]. Hydrogen has the advantage of a high combustion value. The only product of hydrogen combustion is non-polluting water, and hydrogen elements are abundant on Earth. Furthermore, hydrogen can not only be used as a fuel, but also as an energy carrier and storage medium. These advantages make hydrogen a promising new energy source [8].

Currently, hydrogen production is mainly realized by processing petroleum resources, which inevitably generates a huge carbon footprint and requires significant use of non-renewable energy [9]. Electrocatalytic HER has the characteristics of high efficiency, sustainability, and no carbon emissions, making it an ideal method for green hydrogen production [10]. Precious metal catalysts such as Pt [11], Ru [12], Ir [13], Rh [14], and Pd [15] have high catalytic activity, but they are costly, underutilized, and poorly durable [16]. Therefore, finding effective, economical, and durable catalysts is the key to electrocatalytic hydrogen production [17]. In recent years, transition metal catalysts such as Fe [18–20], Co [21–23], Ni [24–26], Mo [27,28], Ti [29,30], and Cu [31–34], which are abundant and inexpensive, have become promising materials in the field of electrocatalytic HER.

As a porphyrin family member, the corrole macrocycle has one fewer *meso*-carbon atom and one more hydrogen atom in the ring compared to porphyrin rings. This makes it a trianionic ligand that can stabilize the central metal ions with a higher oxidation state [35,36]. By introducing electron-withdrawing groups such as halogen [37,38], $-\text{CF}_3$ [39,40], $-\text{C}_6\text{F}_5$ [41,42], and $-\text{CN}$ [43,44] at the *meso*- and/or β -positions of the corrole ring, the electrocatalytic hydrogen performance of metal corroles may be significantly enhanced.

Previously, we have investigated the effect of the *o*-, *m*-, and *p*-hydroxyl group of *meso*-phenyl on the electrocatalytic HER performance of cobalt triaryl corrole complexes [45]. In terms of the electron-withdrawing effect, a nitro group would be more favorable for HER than an electron-donating hydroxyl group. We found that a 5,10,15-tris(4-nitrophenyl)corrole cobalt complex had a better electrocatalytic HER activity than its counterpart cobalt 5,10,15-tris(phenyl)corrole [46]. Cao et al. also reported that the copper corrole bearing nitro group had a better electrocatalytic performance [47]. Here, we wish to report the synthesis of three new cobalt corrole complexes with *o*-nitrobenzyl, *m*-nitrobenzyl, and *p*-nitrobenzyl at the *meso* 10-position of the corrole macrocycle, respectively (Scheme 1), to investigate the effect of the nitro substituent position on their electrocatalytic HER activity in organic and neutral aqueous phases.



Scheme 1. Structure of three complexes 1–3.

2. Results and Discussion

2.1. Structural Characterization

Free-base corroles and cobalt complexes 1–3 were characterized for structure and purity using ultraviolet–visible spectroscopy (UV–vis), high-resolution mass spectroscopy (HRMS), X-ray photoelectron spectroscopy (XPS), and nuclear magnetic resonance spectroscopy (NMR). Corresponding graphs and characterization data are given in the text and Supporting Information (Figures S1–S20).

2.1.1. UV–Vis Spectra of Free-Base Corroles and Cobalt Complexes

As shown in Figure S19, consistent with previous reports [45], the UV–vis of the free-base corroles all have a sharp and high Soret band at around 410 nm and two lower and wider Q-bands at 500–650 nm. The Soret band absorption peaks of the cobalt complexes are blue-shifted, weaker, and split compared to the free-base complexes, indicating that triphenylphosphine is coordinated to cobalt [43].

2.1.2. X-ray Photoelectron Spectroscopy

To further characterize these three cobalt complexes, we determined the elemental composition of them by XPS and determined the valence state of the cobalt element. The XPS full spectra (Figure S20) show that the synthesized cobalt complexes contain Co, F, N, P, C, and O elements. The XPS spectra for Co 2p and N 1s of complexes 1–3 are shown in Figure 1. The peak positions of these complexes are similar, while the peak shape is not exactly the same for all samples. This reflects that complexes 1–3 do have a different electronic structure. It can be found that the $\text{Co}2\text{p}^{1/2}$ binding energies of complexes 1–3 are

795.58, 795.18, and 795.18 eV, respectively, and for $\text{Co}2\text{p}_{3/2}$ are 780.38, 780.38, and 780.18 eV, respectively. This demonstrates that the central cobalt element in all three cobalt complexes is positive trivalent [48]. Among the three complexes, complex 1 has the highest $\text{Co}2\text{p}$ binding energy, indicating that the electron cloud density of Co in complex 1 is the lowest, which may result from the strongest electron-withdrawal effect of the *o*-nitrobenzyl. And these three complexes all have peaks at around 398.7 eV and 406.1 eV, which are, respectively, classified as pyrrole nitrogen and nitro nitrogen [49]. Furthermore, the XPS of $\text{F}1\text{s}$, $\text{P}2\text{p}$, and $\text{O}1\text{s}$ are shown in Figure S20.

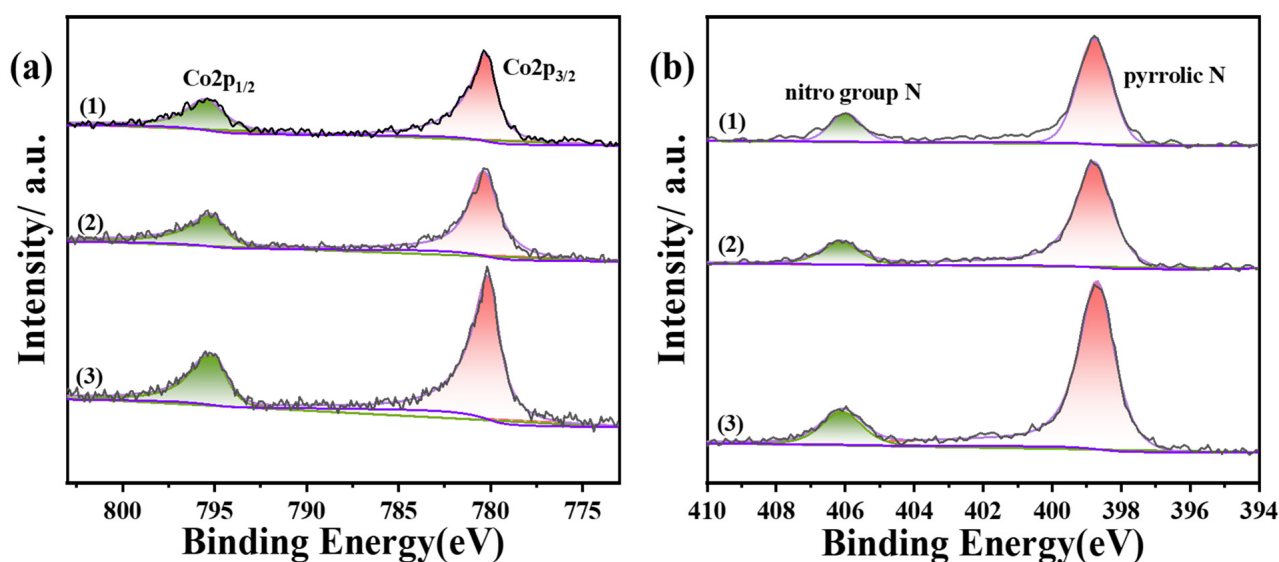


Figure 1. XPS spectra for Co 2p (a), N 1s (b) of complexes 1–3.

2.1.3. X-ray Diffraction of Single Crystal

Single crystals of the complex 1 (CCDC No2326752), 2 (CCDC No2326751), and 3 (CCDC No2326750) were obtained in a mixed system of hexane and dichloromethane using solvent volatilization. The structures of the three single crystals are shown in Figure 2, and some specific data are shown in Tables S1–S3. The structures show that the four pyrrole N atoms of corrole successfully bind to the cobalt atom, and the cobalt complexes are axially coordinated with triphenylphosphine. The cobalt atoms of complexes 1, 2, and 3 have deviation distances from the N4 plane, which are 0.2831 Å, 0.2756 Å, and 0.2721 Å, respectively. The deviation of the cobalt atoms from the N4 plane may be caused by the spatial repulsion of the axial ligand triphenylphosphine. The length of the Co–P bonds is 2.214 Å, 2.204 Å, and 2.206 Å, respectively. And the length ranges of the Co–N bonds in complexes 1, 2, and 3 are 1.857 Å–1.894 Å, 1.866 Å–1.891 Å, and 1.865 Å–1.881 Å, respectively, which indicates that the electronic structure of cobalt in these complexes is $d^6\text{Co}^{\text{III}}$ [50].

2.2. Cyclic Voltammogram Studies

Cyclic voltammograms (CVs) were recorded at a scanning speed of 100 mV/s in a DMF medium with 0.1 M TBAP, calibrated with ferrocene. The three cobalt complexes were preliminarily electrochemically characterized in the $-2.1\sim 0$ V potential range (Figure 3). Table 1 lists the redox peak potentials of the three complexes. Figure 3 shows that complexes 1–3 exhibit the first reduction peak at -0.779 , -0.755 , and -0.735 V, respectively, assigned to the reduction of Co^{III} to Co^{II} . The $\text{Co}^{\text{III}}/\text{Co}^{\text{II}}$ redox couple is irreversible due to the detachment of the axial ligand triphenylphosphine [43]. The potential of the first reduction wave peaks follows an order of $1 < 2 < 3$, showing that the steric effect of the nitro group is the main controlling factor. Possibly, the steric hindrance between the big axial ligand triphenylphosphine and nitro group forces the cobalt atoms to deviate from the corrole N4

plane at different distances, and the deviation is not favored for the metal–ligand aromatic electron communication, thus lowering the electron–withdrawing effect of the nitro group on the central Co atom. This may be further evidenced by the X-ray single–crystal structure. As mentioned in the previous X-ray diffraction single–crystal structures, the distance between the cobalt atom and N4 plane follows an order of $1 > 2 > 3$. Via the comparison of the CVs between the cobalt corrole complexes and free–base corroles, the second reduction peak located at around -1.60 V is the reduction peak of the nitro group. Similarly, the less perturbed nitro group in complex **1** exhibits the most negative reduction potential. The third reduction peaks of complexes **1–3** appear at -1.906 , -1.920 , and -1.909 V, respectively. This reduction wave can be assigned to the reduction of Co^{II} to Co^{I} [51]. This reduction wave potential follows an order of $2 < 1 \sim 3$, showing that the normal electron–withdrawing effect of the nitro groups is mainly controlling the redox potential difference in the $\text{Co}^{\text{II}}/\text{Co}^{\text{I}}$ couple after the axial triphenylphosphine ligand leaves.

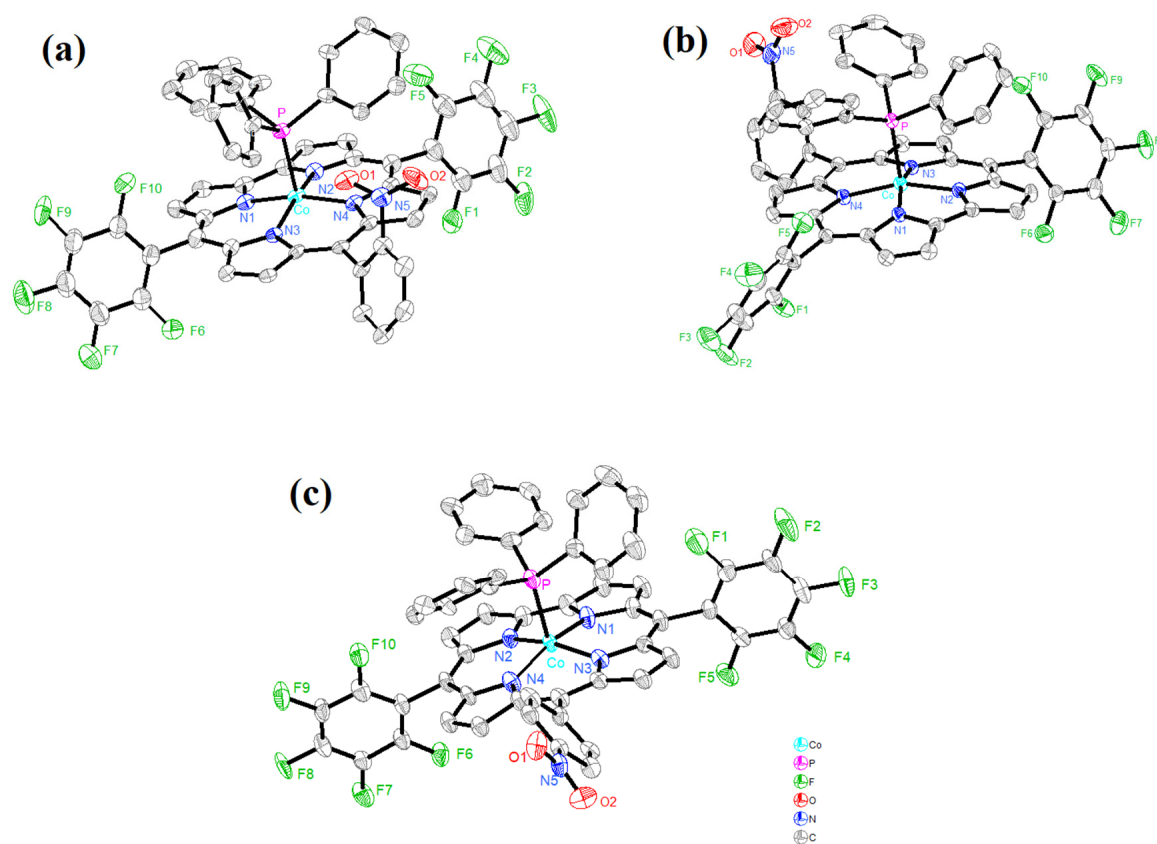


Figure 2. X-ray structure of complexes **1** (a), **2** (b), **3** (c). Thermal ellipsoid plot (50% probability).

Table 1. Redox peak potentials of complexes **1–3** in DMF containing 0.1 M TBAP.

Complex	$\text{Co}^{\text{III}}/\text{Co}^{\text{II}}$		$-\text{NO}_2\text{Ph}$	$\text{Co}^{\text{II}}/\text{Co}^{\text{I}}$	
	Ox 1/V	Red 1/V	Red 2/V	Ox 3/V	Red 3/V
2–NBPC–Co (1)	−0.463	−0.779	−1.671	−1.807	−1.906
3–NBPC–Co (2)	−0.435	−0.755	−1.541	−1.829	−1.920
4–NBPC–Co (3)	−0.415	−0.735	−1.537	−1.813	−1.909

CV tests were conducted on the three complexes in DMF solution at different scan rates in Figure S21. From the figure, it can be seen that the peak current (i_p) is linearly related to the square root of the scan rate ($v^{1/2}$), which indicates that the reaction is controlled by diffusion [52].

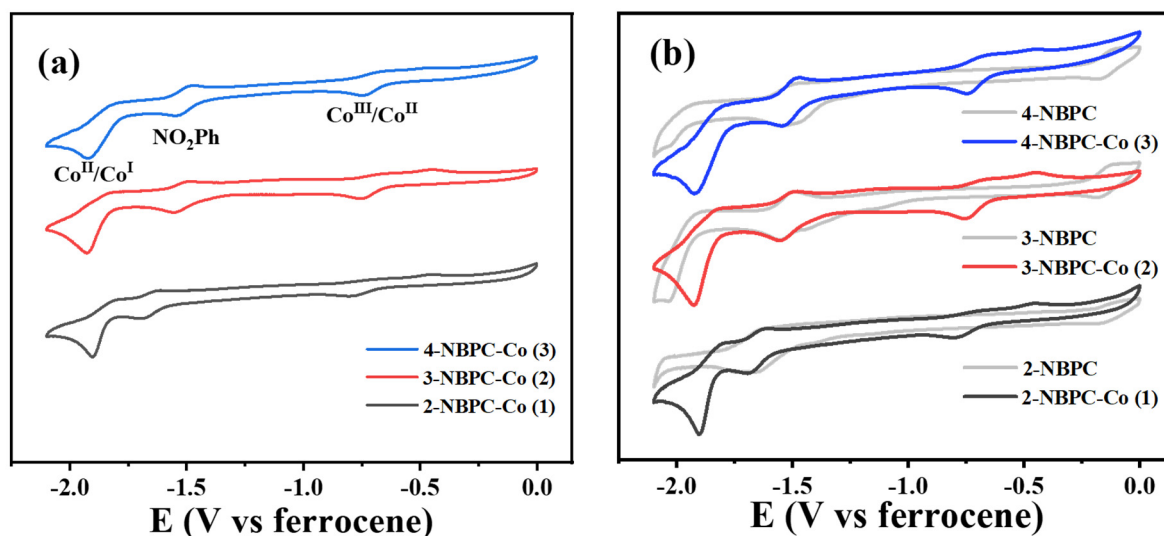


Figure 3. (a) CVs of the complexes 1–3 (0.5 mM) in DMF (0.1 M TBAP); (b) CVs comparison between complexes 1–3 and their free-base corroles.

2.3. Electrocatalytic Study in DMF

Due to the influence of proton sources on the catalytic pathway and property of catalysts, acetic acid (AcOH, pKa 13.2 in DMF [53]), trifluoroacetic acid (TFA, pKa 3.5 in DMF [52]), and *p*-toluenesulfonic acid (TsOH, pKa 2.6 in DMF [53]) were used as the proton sources to study the electrocatalytic HER catalytic activeness of the three complexes in DMF.

In Figure S22, AcOH was used as the proton source. With the addition of AcOH, the first redox peak of the $\text{Co}^{\text{III}}/\text{Co}^{\text{II}}$ couple of the three complexes is almost unchanged, while the reduction peak current of the NO_2Ph group increases obviously but does not change with the increasing acid concentration. And the third reduction peak of $\text{Co}^{\text{II}}/\text{Co}^{\text{I}}$ shifts slightly positively. However, the catalytic current is small, suggesting that the electrocatalytic capacity is not good in weak acidic.

As shown in Figure 4, the electrocatalytic HER performance of the three complexes was investigated using a medium-strength acid TFA as the proton source. The redox peak of the $\text{Co}^{\text{III}}/\text{Co}^{\text{II}}$ pair of these three complexes remains unchanged with the increasing acid concentration, which means that this process only involves the $\text{Co}^{\text{III}}/\text{Co}^{\text{II}}$ reduction accompanying the detachment of triphenylphosphine [54]. The reduction peak potential of the NO_2Ph group significantly shifts positively with the increase in the acid concentration. However, the reduction peak current basically stays unchanged, suggesting that the NO_2Ph group is involved in the pure redox reaction only [55]. The reduction peak current of the $\text{Co}^{\text{II}}/\text{Co}^{\text{I}}$ pair decreases a little when the acid addition is only 2 eq, but the peak potential is positively shifted. When more acid is added, the oxidation peak of the $\text{Co}^{\text{II}}/\text{Co}^{\text{I}}$ pair gradually disappears. Meanwhile, the reduction peak current increases remarkably with the increase in the acid concentration, indicating that the catalytic HER process occurs, and Co^{I} is the active center of HER [43]. It can be seen that Co^{II} obtains an electron to be reduced to Co^{I} , which is then protonated to form a transient $\text{Co}^{\text{I}}-\text{H}^+$ species, which then will quickly transform to a $\text{Co}^{\text{III}}-\text{H}^-$ intermediate. Finally, this intermediate reacts with a proton to produce H_2 [39]. The performance of the catalysts is further evaluated using $i_{\text{cat}}/i_{\text{p}}$, where i_{cat} is the reduction peak current with the addition of acid and i_{p} is the reduction peak current without acid; the $i_{\text{cat}}/i_{\text{p}}$ values of the three complexes in TFA are given in Figure 4, and the ranking of the $i_{\text{cat}}/i_{\text{p}}$ values of the three complexes is $1 > 3 > 2$.

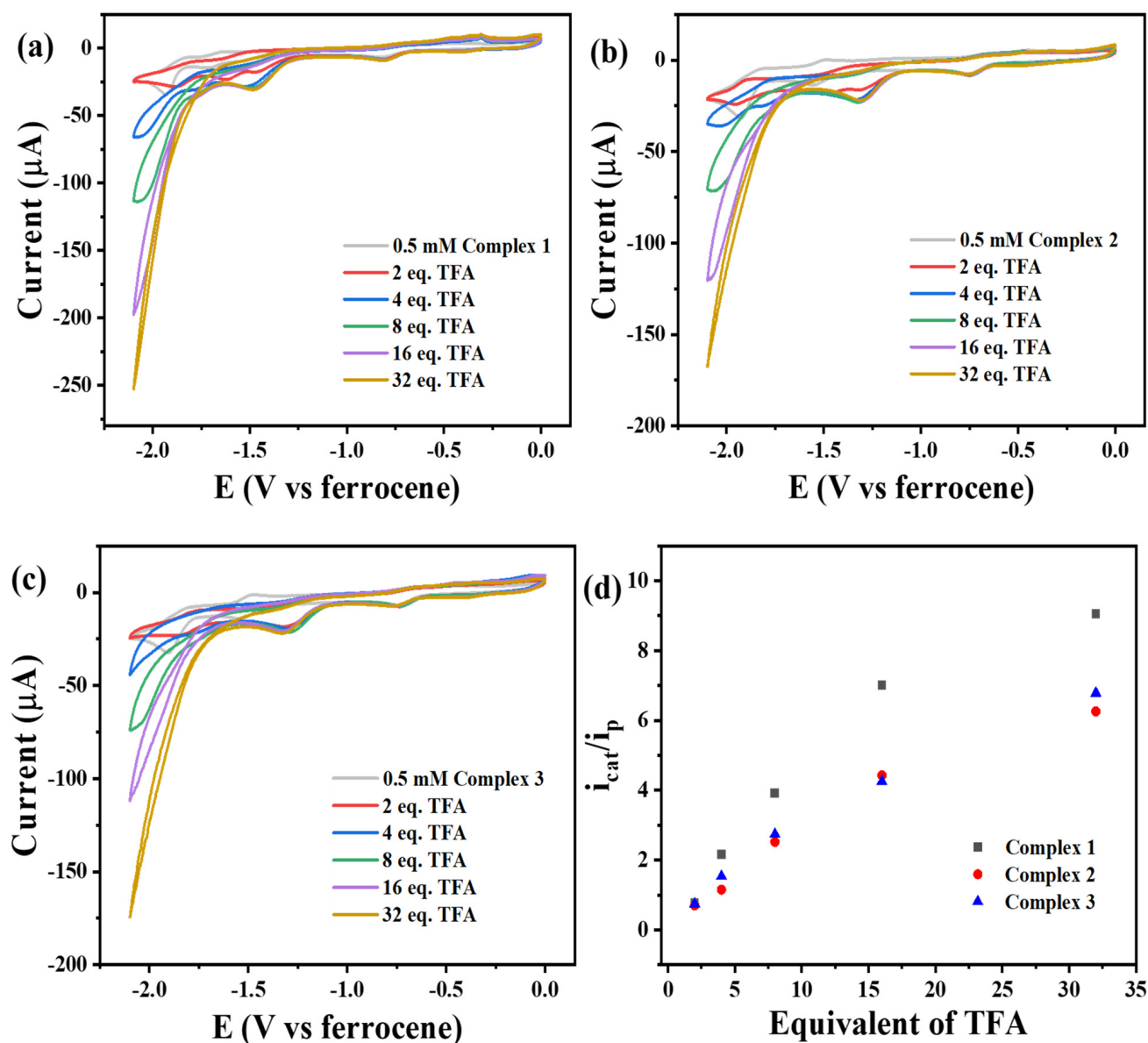


Figure 4. CVs of 0.5 mM **1** (a), **2** (b), and **3** (c) in DMF (0.1 M TBAP); i_{cat}/i_p values at different TFA concentrations (d).

Further, the electrocatalytic HER property of the three complexes was investigated using TsOH as the proton source. In Figure 5, similar to TFA, the redox peak of the $\text{Co}^{\text{III}}/\text{Co}^{\text{II}}$ electric pair of all three complexes does not change with the acid concentration. The reduction peak of the NO_2Ph group is only an electron transfer reaction and is not involved in proton-coupling processes. When the addition of acid is only 2 eq, the reduction peak potential of $\text{Co}^{\text{II}}/\text{Co}^{\text{I}}$ may be observed to be positively shifted. With the increasing acid concentration, the peak current increases remarkably, implying that after Co^{II} obtains an electron to form Co^{I} , the Co^{I} will soon couple with a proton to form a transient $\text{Co}^{\text{I}}-\text{H}^+$ which then will quickly transform to a $\text{Co}^{\text{III}}-\text{H}^-$ intermediate. After that, this intermediate combines with a proton to eventually produce H_2 . In Figure 5d, the i_{cat}/i_p values of the three complexes are also ranked as $1 > 3 > 2$.

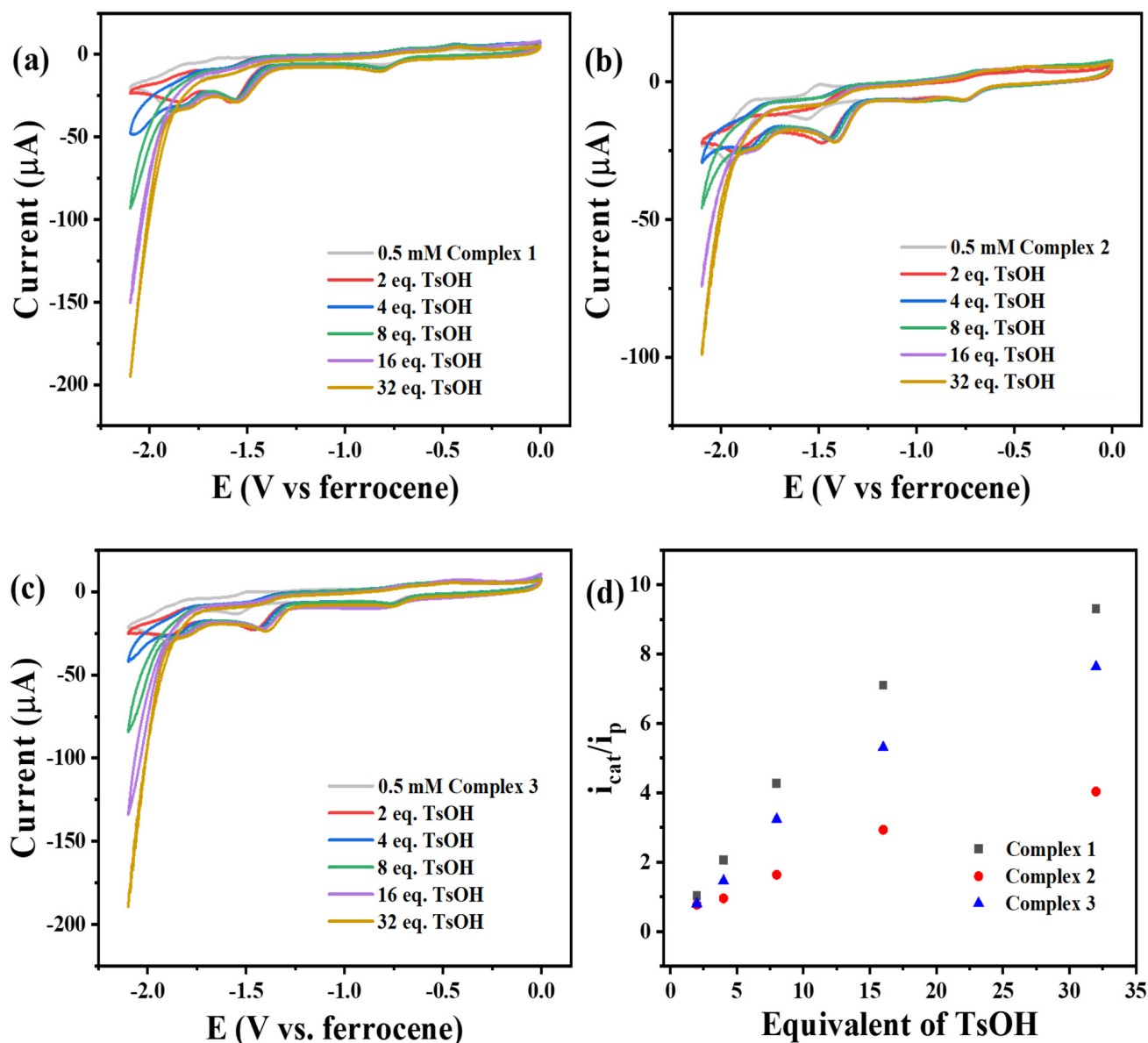


Figure 5. CVs of 0.5 mM **1** (a), **2** (b), and **3** (c) in DMF (0.1 M TBAP); i_{cat}/i_p values at different TsOH concentrations (d).

Equations (1) and (2) and the Tafel Equation (3) were further used to calculate the Tafel slope to investigate the catalytic dynamics of the complexes and the results are shown in Figure S23. The relevant Tafel data are summarized in Table S4. In DMF with 32 eq. TFA, the Tafel slopes of complexes 1–3 are 31, 49, and 41 mV dec^{-1} , respectively. In DMF with 32 eq. TsOH, the Tafel slopes of complexes 1–3 are 34, 43, and 39 mV dec^{-1} , respectively; it can be seen that the Tafel slope is $1 < 3 < 2$, indicating that the kinetic superiority of the electrocatalytic HER is $1 > 3 > 2$.

$$\eta = E_{HA}^0 - E \quad (1)$$

$$E_{HA}^0 = E_{H^+}^0 - \left(\frac{2.303RT}{F} \right) pK_{aHA} \quad (2)$$

$$\eta = b \log j + a \quad (3)$$

where η is the overpotential, E_{HA}^0 is the standard electrode potential of H^+/H_2 , $E_{H^+}^0 = -0.62$ V vs. ferrocene in DMF, pK_{aHA} is the dissociation constant of acid in solvent, $E_{TFA}^0 = -0.83$ V, $E_{TsOH}^0 = -0.78$ V, b is the Tafel slope, j is the current density, and a is a constant [56,57].

Figure S24 tested the CV curves of the bare glassy carbon electrode, free-base corrole 2–NBPC, and complex **1** (2–NBPC–Co) under the condition of adding an equal amount of acid in the DMF system and compared it with the current value of the bare glassy carbon electrode without the acid addition. It can be seen that after adding acid, the current of the bare glassy carbon electrode increases very little, and the catalytic current of 2–NBPC is obvious but far less than that of complex **1**. The result suggests that the significant increase in the catalytic current is attributed to the cobalt complexes.

In a nitrogen environment, controlled potential electrolysis experiments were conducted on the three complexes in DMF with excessive TFA at the potential of -2.1 V for 1 h. Deducting the blank, the rank of charge accumulation is found to be $\mathbf{1} > \mathbf{3} > \mathbf{2}$, with a maximum accumulated charge of 0.54 C (Figure S25). Equation (4) was used to calculate the TOF values of the three cobalt complexes; the results are summarized in Table S5 [58]. Furthermore, the UV–vis results of complexes **1–3** before and after electrolysis show that these catalysts all have good stability (Figure S26). The 20–turn cyclic voltametric scanning of the three complexes showed no significant change in the CV curves between the 1st and 20th turns, which also indicates the good stability of the complexes (Figure S27). The glassy carbon electrodes that were continuously electrolyzed in the catalyst for 1 h were briefly rinsed and then the CV curves of the bare glassy carbon electrodes were tested. Comparing the CV curves of the bare glassy carbon electrodes before and after electrolysis (Figure S28), it can be seen that there is no deposition of electrochemical active substances on the surface of the glassy carbon electrodes.

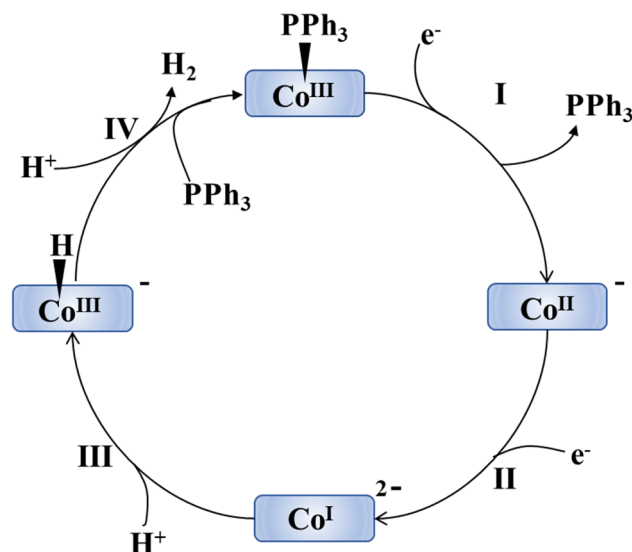
$$\text{TOF} = \frac{\Delta C}{F \cdot n_1 \cdot n_2 \cdot t} \quad (4)$$

where ΔC is the amount of charge accumulated in the experiment after subtracting the blanks, F is the Faraday constant, n_1 is the number of electrons needed to produce 1 mole of hydrogen, n_2 is the amount of catalyst, and t is the electrolysis time.

In Figure S29, the catalytic effect of complexes **1–3** was further investigated using electrochemical impedance spectroscopy (EIS) at the potential of -1.7 V. In DMF solution containing 32 eq. TFA, the series resistance R_s values of the complexes **1**, **2**, and **3** are 34–39 Ω , and the charge transfer resistance R_{ct} values are 517.1, 596.0, and 560.7 Ω , respectively. In DMF solution containing 32 eq. of TsOH, the R_s values of complexes **1**, **2**, and **3** are 32–36 Ω , and the R_{ct} values are 407.4, 571.0, and 437.1 Ω , respectively. The R_{ct} values in different systems were summarized in Table S6. The low R_s indicates that the catalytic system is a homogeneous catalytic process, and the lower R_{ct} means that the electrocatalysis has a stronger charge transfer capability and is more favorable for HER. In both proton sources, the R_{ct} values are $\mathbf{1} < \mathbf{3} < \mathbf{2}$.

2.4. Possible Catalytic Hydrogen Production Pathways

On the basis of the above experiments and studies, the electrocatalytic HER mechanism for the three catalysts in the organic phase with TFA and TsOH as the proton sources is hypothesized in Scheme 2. The $\text{Co}^{\text{III}}/\text{Co}^{\text{II}}$ reduction wave is nearly not changed with increasing the acid concentration, indicating that this step is a pure one–electron reduction of Co^{III} to Co^{II} , which is an E process. Meanwhile, the reduction peak current of the $\text{Co}^{\text{II}}/\text{Co}^{\text{I}}$ pairs increases significantly with the increase in the acid concentration, showing when Co^{II} obtained an electron to form Co^{I} , it will soon bind with a proton to form transient $\text{Co}^{\text{I}}-\text{H}^+$, which will transform to a $\text{Co}^{\text{III}}-\text{H}^-$ hydride intermediate, and this is an EC process. Finally, the $\text{Co}^{\text{III}}-\text{H}^-$ hydride reacts with a proton to produce H_2 , which is a C process. Therefore, the possible catalytic route is the EECC pathway (I–IV, in Scheme 2).



Scheme 2. Possible pathways for the electrocatalytic HER of complexes 1–3 when TFA or TsOH are used as proton sources.

2.5. Electrocatalytic Study in Neutral Aqueous System

To examine the practicality of the three complexes, the HER performance of the three catalysts was tested in 0.1 M phosphate buffer ($V_{\text{MeCN}}/V_{\text{H}_2\text{O}} = 2/3$) of pH = 7. MeCN was applied to improve the solubility of the complexes in H_2O . Ag/AgCl was chosen as the reference electrode for all tests. The effect of the cobalt corrole concentration on the HER in the neutral aqueous system was investigated in Figure S30. The figure suggests that the catalytic current increases gradually with the increase in the cobalt complex concentration. In Figure 6, the catalytic current is extremely small when the catalyst is not added. After the addition of the three cobalt complexes, significant catalytic currents appear in the CV tests; among the three complexes, the catalytic currents of complex 1 are the largest. And the addition of the cobalt complexes results in a large positive shift in the onset potential, indicating that these three complexes have a significant electrocatalytic HER property in this system. The Tafel slopes of the three complexes, as shown in Figure S31, are 99, 114, and 111 mV dec^{-1} , respectively, and the data have been summarized in Table S4.

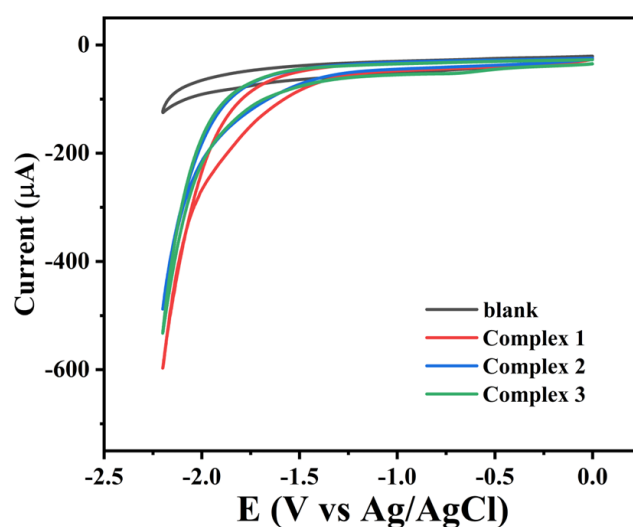


Figure 6. CVs of complexes 1–3 (2.5 μM) in aqueous neutral system.

In addition, two-minute controlled potential electrolysis experiments were carried out on three cobalt complexes at overpotentials of 838–1238 mV in Figure S32 (blanks have been

eliminated in all data). The results show that the charge accumulation of complex 1 is the largest, reaching about 120 mC at 1238 mV. The TOF values of the three cobalt complexes at different overpotentials were calculated using Equations (1) and (5) [55]. It can be seen from Figure S31(d) that the turnover frequency (TOF) values of the three cobalt complexes increase with the increasing overpotential, and the TOF values at 938 mV for 1, 2, and 3 are 137.40, 126.24, and 128.10 h^{-1} , respectively, the specific results are summarized in Table S5. Table S7 compares the TOF values of these three new complexes with other reported cobalt complexes, and the new complexes are found to have good property [39,45,51,57,59,60].

$$\text{Overpotential} = \text{Applied potential} + 0.059 \text{ pH} + 0.199 \text{ V} \quad (5)$$

At the initial potential of -1.4 V , the electrocatalytic performance of the three complexes was studied using electrochemical impedance spectroscopy (EIS). The R_s values of complexes 1–3 are 15–18 Ω , and the R_{ct} values are 159.9, 187.8, and 166.9 Ω , respectively (Figure S33). The relevant data are listed in Table S6.

Other conditions were kept constant, and the electrolyte of the 0.25 M complex was continuously electrolyzed at -1.70 V for 1 h. In Figure 7, the gases produced are collected and analyzed qualitatively and quantitatively by gas chromatography. After subtracting blanks, the volume of H_2 produced is calculated to be 0.17 mL, 0.20 mL, and 0.35 mL using the external standard method (Figure S34). The Faraday efficiencies of the three catalysts are evaluated using Equations (6) [57] and are calculated to be 86.92%, 81.39%, and 85.72%, respectively.

$$\text{Faradaic efficiency for } \text{H}_2 = \frac{F \cdot n_{\text{H}_2} \cdot z}{Q} \times 100\% \quad (6)$$

where F is the Faraday constant, n_{H_2} is the amount of H_2 produced by electrolysis, z is the number of electrons required to produce 1 mol of H_2 , and Q is the accumulated charge in electrolysis.

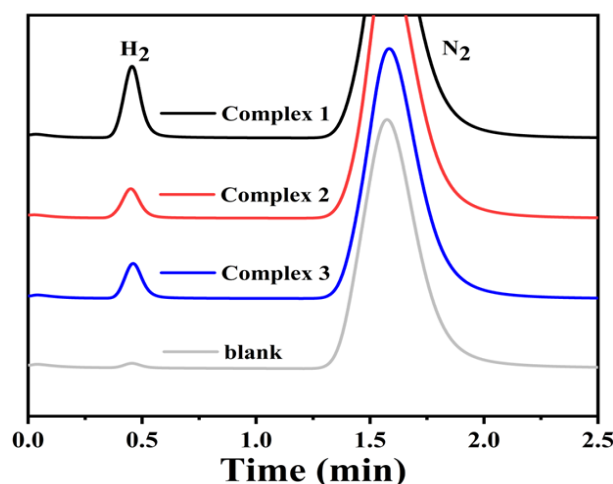


Figure 7. Gas chromatogram of complexes 1–3 after electrolysis at -1.7 V for 1 h.

Figure S35 investigates the stability of the three complexes by measuring the current density changes during continuous electrolysis at a -1.7 V potential for 8 h. It is clear that the current density values of complexes 1–3 remain basically constant throughout the entire 8 h stability test, which indicate that these three complexes have good electrocatalytic stability. In order to make the potentials of the two systems more comparable, some current values with the same NHE scale of 2 V in the CV tests of the two systems are summarized in Table S8 [61].

3. Materials and Methods

All reagents were commercially available and were used without further purification, unless otherwise stated. Bruker Avance III NMR spectrometer was used to measure the H and F spectra in CDCl₃ solvent. High-resolution mass spectra (HRMS) were determined by Agilent 1290LC-MS. MeOH and THF were used as solvents, and electrospray ionization (ESI) source was used as the light source. UV-vis was measured at r. t. using a Hitachi U-3010 spectrophotometer with CH₂Cl₂ as the solvent. X-ray photoelectron spectra (XPS) were tested with Thermo Scientific K-Alpha, and the associated binding energy was corrected with a C1s peak (284.8 eV). X-ray diffraction of single crystals was measured using Bruker D8 VENTURE. All electrochemical tests were conducted using the CHI-660E electrochemical workstation. Organic-phase electrochemical tests were conducted using a DMF solution of tetrabutylammonium perchlorate (TBAP) as the supporting electrolyte, with Ag/AgNO₃ as the reference electrode, glassy carbon as the working electrode, and graphite rod as the counter electrode. The aqueous neutral system was a solution of a mixture of MeCN and H₂O with a volume ratio of 2:3, and KCl, KOH, and KH₂PO₄ were added, with Ag/AgCl as the reference electrode, glassy carbon as the working electrode, and platinum wire as the counter electrode.

Synthesis of 10-(2-nitrophenyl)-5,15-bis-pentafluorophenyl corrole (2-NBPC)

As is shown in Figure 8, the synthesis could be divided into two steps; the first was the synthesis of pentafluorophenyl dipyrromethane. Pentafluorobenzaldehyde (5.6 g) and newly distilled pyrrole (320 mL) were stirred evenly, then catalyst TFA (240 μL) was added and stirred at r. t. for 2 h. Then, Et₃N (480 μL) was added to terminate the reaction, and after the white smoke in the bottle disappeared, a black oily liquid was obtained by vacuum distillation. Then, this liquid was purified by a silica column with DCM:HEX = 1:1 eluent, and beige solid was obtained as pentafluorophenyl dipyrromethane (6.9 g, 77%).

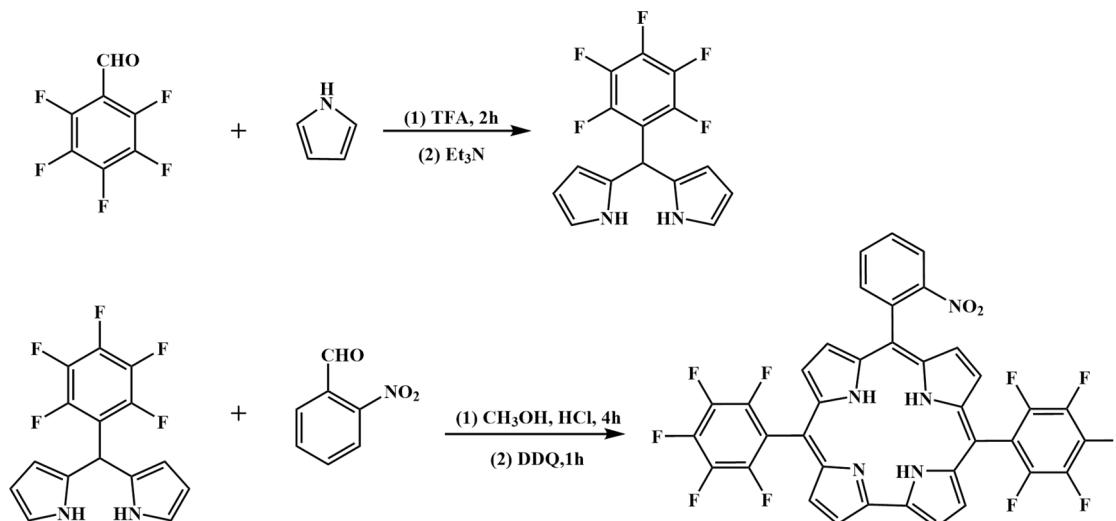


Figure 8. Schematic of the synthesis of 2-NBPC.

The second step was to synthesize the target product. 2-Nitrobenzaldehyde (0.15 g) and pentafluorophenyl dipyrromethane (0.63 g) were added in MeOH (100 mL), then HCl (3.6%, 100 mL) was added and the mixture was stirred at r. t. for 4 h. The organic phase was then extracted with DCM and H₂O and dried with anhydrous sodium sulfate. Then, DDQ was added for 1 h. Next, it was purified by a silica column with DCM:HEX = 2:1 eluent to separate the impurities, and finally recrystallized with DCM and HEX to obtain a high-purity product as 10-(2-nitrophenyl)-5,15-bis-pentafluorophenyl corrole (2-NBPC) (230 mg, 31%). HRMS (ESI) [M + H]⁺, calculated for C₃₇H₁₅F₁₀N₅O₂: 752.1139, found 752.1147. ¹H NMR (400 MHz, Chloroform-d) δ 9.10 (d, *J* = 4.3 Hz, 2H), 8.70 (d, *J* = 4.7 Hz, 2H), 8.56 (d, *J* = 4.3 Hz, 2H), 8.50 (d, *J* = 4.8 Hz, 2H), 8.39 (m, 1H), 8.24–8.19 (m, 1H), 8.00–7.92

(m, 2H). ^{19}F NMR (376 MHz, Chloroform-*d*) δ -137.23 (2F), -138.08 (2F), -152.61 (2F), -161.49 (2F), -161.77 (2F).

Synthesis of 10-(3-nitrophenyl)-5,15-bis-pentafluorophenyl corrole (3-NBPC)

Similar to 2-NBPC, after recrystallization from DCM/Hex, obtain pure corrole (246 mg, yield 33%). HRMS (ESI) $[\text{M} + \text{H}]^+$, calculated for $\text{C}_{37}\text{H}_{15}\text{F}_{10}\text{N}_5\text{O}_2$: 752.1139, found 752.1153. ^1H NMR (400 MHz, Chloroform-*d*) δ 9.15 (d, $J = 4.3$ Hz, 2H), 9.04 (t, $J = 2.0$ Hz, 1H), 8.77 (d, $J = 4.7$ Hz, 2H), 8.64 (dd, $J = 8.3, 2.5$ Hz, 1H), 8.60 (d, $J = 4.7$ Hz, 4H), 8.51 (d, $J = 7.7$ Hz, 1H), 7.96 (t, $J = 7.9$ Hz, 1H). ^{19}F NMR (376 MHz, Chloroform-*d*) δ -137.83 (4F), -152.36 (2F), -161.50 (4F).

Synthesis of 10-(4-nitrophenyl)-5,15-bis-pentafluorophenyl corrole (4-NBPC)

Similar to 2-NBPC, after recrystallization from DCM/Hex, obtain pure corrole (258 mg, yield 35%). HRMS (ESI) $[\text{M} + \text{H}]^+$, calculated for $\text{C}_{37}\text{H}_{15}\text{F}_{10}\text{N}_5\text{O}_2$: 752.1139, found 752.1149. ^1H NMR (400 MHz, Chloroform-*d*) δ 9.13 (d, $J = 4.3$ Hz, 2H), 8.77 (d, $J = 4.8$ Hz, 2H), 8.65–8.58 (m, 6H), 8.36 (d, $J = 8.5$ Hz, 2H). ^{19}F NMR (376 MHz, Chloroform-*d*) δ -137.86 (4F), -152.29 (2F), -161.46 (4F).

Synthesis of complex 1

As is shown in Figure 9, 2-NBPC (100 mg) and sodium acetate (200 mg) were added in MeOH (60 mL) and DCM (60 mL), then triphenylphosphine (330 mg) was added, and finally cobalt acetate tetrahydrate (200 mg) was added and reacted at r. t. for 1 h. The solution was then extracted with DCM and saturated saline, then the organic phase was collected. After drying, the crude product was purified by a silica column with the eluent of DCM:HEX = 2:1, and brown solid was obtained. Finally, after recrystallization with DCM and HEX, a high purity cobalt complex product (130 mg, 91%) was obtained (130 mg, 91%). HRMS (ESI) $[\text{M} + \text{H}]^+$, calculated for $\text{C}_{55}\text{H}_{27}\text{CoF}_{10}\text{N}_5\text{O}_2\text{P}$: 1070.1147, found 1070.1172. ^1H NMR (400 MHz, Chloroform-*d*) δ 8.60 (d, $J = 4.5$ Hz, 2H), 8.33–8.20 (m, 5H), 8.08–7.99 (m, 3H), 7.85 (m, 2H), 7.05 (t, $J = 7.2$ Hz, 3H), 6.70 (d, $J = 6.3$ Hz, 6H), 4.67 (m, 6H). ^{19}F NMR (376 MHz, Chloroform-*d*) δ -136.03–-138.03 (4F), -154.02 (2F), -161.65–-162.89 (4F).

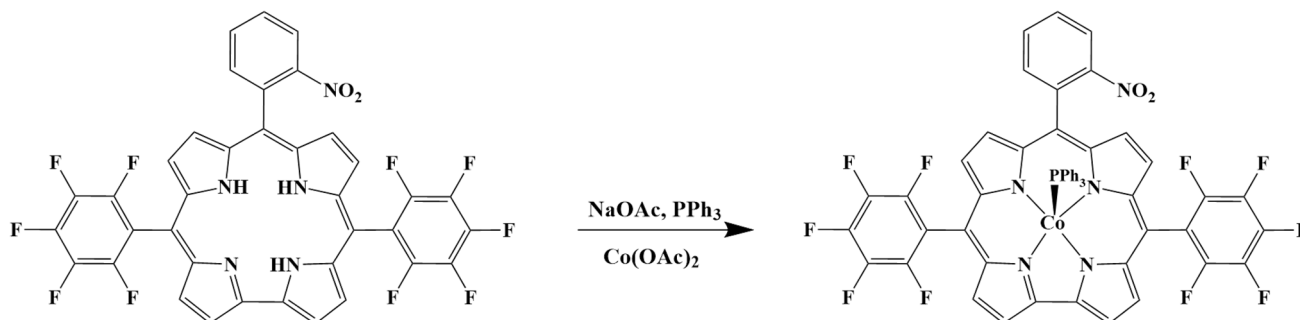


Figure 9. Schematic of the synthesis of Complex 1.

Synthesis of complex 2

Similar to complex 1, after recrystallization, obtain pure cobalt complex (138 mg, yield 97%). HRMS (ESI) $[\text{M} + \text{H}]^+$, calculated for $\text{C}_{55}\text{H}_{27}\text{CoF}_{10}\text{N}_5\text{O}_2\text{P}$: 1070.1147, found 1070.1148. ^1H NMR (400 MHz, Chloroform-*d*) δ 8.84 (dd, $J = 26.2, 4.6$ Hz, 2H), 8.59–8.55 (m, 1H), 8.38 (d, $J = 7.5$ Hz, 1H), 8.34 (d, $J = 3.3$ Hz, 2H), 8.21 (d, $J = 4.8$ Hz, 1H), 8.17 (d, $J = 4.7$ Hz, 2H), 8.10 (t, $J = 5.2$ Hz, 2H), 7.84 (t, $J = 7.9$ Hz, 1H), 7.10 (m, 3H), 6.74 (m, 6H), 4.63 (dd, $J = 10.5, 8.2$ Hz, 6H). ^{19}F NMR (376 MHz, Chloroform-*d*) δ -136.68–-138.00 (4F), -153.80 (2F), -161.57–-162.61 (4F).

Synthesis of complex 3

Similar to complex 1, after recrystallization, obtain pure cobalt complex (133 mg, yield 93%). HRMS (ESI) $[\text{M} + \text{H}]^+$, calculated for $\text{C}_{55}\text{H}_{27}\text{CoF}_{10}\text{N}_5\text{O}_2\text{P}$: 1070.1147, found 1070.1139.

^1H NMR (400 MHz, Chloroform-*d*) δ 8.79 (d, $J = 4.5$ Hz, 2H), 8.52 (dd, $J = 8.3, 2.4$ Hz, 1H), 8.46 (dd, $J = 8.4, 2.4$ Hz, 1H), 8.30 (d, $J = 4.6$ Hz, 2H), 8.24 (d, $J = 7.6$ Hz, 1H), 8.19 (d, $J = 4.8$ Hz, 2H), 8.07 (d, $J = 4.5$ Hz, 2H), 7.56 (d, $J = 8.1$ Hz, 1H), 7.09–7.02 (t, 3H), 6.69 (td, $J = 7.8, 2.6$ Hz, 6H), 4.59 (dd, $J = 11.1, 7.8$ Hz, 6H). ^{19}F NMR (376 MHz, Chloroform-*d*) δ –136.92 (2F), –137.86 (2F), –153.74 (2F), –161.77 (2F), –162.35 (2F).

4. Conclusions

In this paper, three free-base corroles bearing one *o*-, *m*-, or *p*-nitrobenzyl and two pentafluorophenyl groups and their cobalt complexes had been synthesized. The electrocatalytic HER property of these cobalt corrole complexes had also been investigated in a DMF and MeCN/ H_2O system, respectively. The results showed that the prepared three cobalt corroles exhibited significant catalytic activity in both organic and neutral aqueous systems. In the organic phase, the electrocatalytic HER may via the EECC pathway when using TFA and TsOH as the proton sources. And the HER turnover frequency values are up to 137.4 h^{-1} at 938 mV overpotential in the neutral aqueous system. The three cobalt corroles also show good stability in the aqueous neutral system. In both systems, the HER activity follows an order of $1 > 3 > 2$. This is in accordance with the order of the electron-withdrawing effect of the nitro groups on phenyl *ortho*- $\text{NO}_2 > \textit{para}$ - $\text{NO}_2 > \textit{meta}$ - NO_2 , showing the electronic effect of the nitro group on the phenyl of current cobalt tri-phenyl corrole is the main factor controlling the HER activity of them.

Supplementary Materials: The following supporting information can be downloaded at: <https://www.mdpi.com/article/10.3390/catal14070454/s1>, Figure S1: ^1H NMR spectrum of 2-NBPC; Figure S2: ^{19}F NMR spectrum of 2-NBPC; Figure S3: ESI–HRMS spectrum of 2-NBPC; Figure S4: ^1H NMR spectrum of 3-NBPC; Figure S5: ^{19}F NMR spectrum of 3-NBPC; Figure S6: ESI–HRMS spectrum of 3-NBPC; Figure S7: ^1H NMR spectrum of 4-NBPC; Figure S8: ^{19}F NMR spectrum of 4-NBPC; Figure S9: ESI–HRMS spectrum of 4-NBPC; Figure S10: ^1H NMR spectrum of complex 1; Figure S11: ^{19}F NMR spectrum of complex 1; Figure S12: ESI–HRMS spectrum of complex 1; Figure S13: ^1H NMR spectrum of complex 2; Figure S14: ^{19}F NMR spectrum of complex 2; Figure S15: ESI–HRMS spectrum of complex 2; Figure S16: ^1H NMR spectrum of complex 3; Figure S17: ^{19}F NMR spectrum of complex 3; Figure S18: ESI–HRMS spectrum of complex 3; Figure S19: UV–vis spectra of 2-NBPC and 2-NBPC–Co (1) (a), 3-NBPC and 3-NBPC–Co (2) (b), 4-NBPC and 4-NBPC–Co (3) (c) in DCM; Figure S20: XPS survey spectrum (a), XPS spectra of F 1s (b), P 2p (c), and O 1s (d) of complexes 1–3; Figure S21: CVs of 0.5 mM complexes 1 (a), 2 (b), and 3 (c) in a varying scan rate (v) from 100 mV/s to 350 mV/s; plot of peak current (i_p) values of complexes 1 (d), 2 (e), 3 (f) versus the square root of the scan rate ($v^{1/2}$); Figure S22: CVs of 0.5 mM complexes 1 (a), 2 (b), and 3 (c) in DMF (0.1 M TBAP); Figure S23: Tafel plots of the 0.5 mM complexes 1–3 with 32 eq. TFA (a), and 32 eq. TsOH (b) in DMF; Figure S24: CVs of bare glassy carbon electrode without TFA (black), bare glassy carbon electrode (red), 0.5 mM 2-NBPC (blue), and 0.5 mM 2-NBPC–Co (1) (green) with 32 eq TFA in DMF; Figure S25: charge of 0.5 mM complexes 1, 2, and 3 after 1 h of electrolysis in DMF with excessive TFA; Figure S26: UV–vis of complexes 1 (a), 2 (b), and 3 (c) before and after 1 h of electrolysis in excessive TFA; Figure S27: the 1st circle (black line) and the 20th circle (red line) CVs of complexes 1 (a), 2 (b), and 3 (c); Figure S28: comparison of CV curves of bare glassy carbon electrodes before and after electrolysis of complexes 1 (a), 2 (b), and 3 (c) in 32 eq TFA for 1 h; Figure S29: the Nyquist plot of the 0.5mM complexes 1–3 with 32 eq TFA (a), and 32 eq TsOH (b) in DMF; Figure S30: CVs of different concentrations of complexes 1 (a), 2 (b), and 3 (c) in neutral aqueous system ($V_{\text{MeCN}}/V_{\text{H}_2\text{O}} = 2/3$); Figure S31: the Tafel slope of the 0.25 μM complexes 1–3 in neutral aqueous medium ($V_{\text{MeCN}}/V_{\text{H}_2\text{O}} = 2/3$); Figure S32: charges accumulated by electrolysis of 2.5 μM complexes 1 (a), 2 (b), and 3 (c) at different potentials for two minutes and corresponding TOF values (d); Figure S33: the Nyquist plot of the 0.25 μM complexes 1–3 in neutral aqueous medium ($V_{\text{MeCN}}/V_{\text{H}_2\text{O}} = 2/3$); Figure S34: the standard curve of hydrogen volume; Figure S35: timed current measurements of 2.5 μM complexes 1 (a), 2 (b), and 3 (c) electrolyzed at -1.7 V for 8 h in neutral aqueous system; Table S1: crystal data and structure refinement for complex 1; Table S2: crystal data and structure refinement for complex 2; Table S3: crystal data and structure refinement for complex 3; Table S4: Tafel slope in different systems; Table S5: TOF values at different conditions; Table S6:

charge transfer resistance (R_{ct}) in different systems; Table S7: comparison of TOF value of cobalt corroles; [39,45,51,57,59,60]; Table S8: some current values at −2.00 V vs. NHE.

Author Contributions: Conceptualization, J.Z. and H.-Y.L.; visualization, X.-Y.C., S.-Y.X. and Y.-F.Q.; writing—original draft preparation, J.Z.; writing—review and editing, H.-Y.L.; supervision, H.-Y.L., L.-P.S. and J.-Y.C. All authors have read and agreed to the published version of the manuscript.

Funding: This research was funded by the National Natural Science Foundation of China (No. 22005052, 20161068) and the Research Fund Program of Guangdong Provincial Key Laboratory of Fuel Cell Technology (Grant No. FC202211).

Data Availability Statement: The data that support the findings of this study are available from the Supplementary Materials.

Acknowledgments: We thank the School of Chemistry and Chemical Engineering of South China University of Technology for their generous support.

Conflicts of Interest: The authors declare no conflicts of interest.

References

1. Martins, F.; Felgueiras, C.; Smitkova, M.; Caetano, N. Analysis of Fossil Fuel Energy Consumption and Environmental Impacts in European Countries. *Energies* **2019**, *12*, 964. [CrossRef]
2. Liu, Y.; Lu, M.; Perng, T.; Chen, L. Plasmonic enhancement of hydrogen production by water splitting with CdS nanowires protected by metallic TiN overlayers as highly efficient photocatalysts. *Nano Energy* **2021**, *89*, 106407. [CrossRef]
3. Li, S.; Feng, K.; Li, M. Identifying the main contributors of air pollution in Beijing. *J. Clean. Prod.* **2017**, *163*, S359–S365. [CrossRef]
4. Lott, M.C.; Pye, S.; Dodds, P.E. Quantifying the co-impacts of energy sector decarbonisation on outdoor air pollution in the United Kingdom. *Energy Policy* **2017**, *101*, 42–51. [CrossRef]
5. Wu, Z.; Adebayo, T.S.; Alola, A.A. Renewable energy intensity and efficiency of fossil energy fuels in the nordics: How environmentally efficient is the energy mix? *J. Clean. Prod.* **2024**, *438*, 140711. [CrossRef]
6. Zabelin, D.; Tomšíková, K.; Zabelina, A.; Stastny, M.; Michalcova, A.; Mestek, S.; Burtsev, V.; Guselnikova, O.; Miliutina, E.; Kolska, Z.; et al. Enhancing hydrogen storage efficiency: Surface-modified boron nanosheets combined with IRMOF-20 for safe and selective hydrogen storage. *Int. J. Hydrogen Energy* **2024**, *57*, 1025–1031. [CrossRef]
7. Ishaq, H.; Dincer, I.; Crawford, C. A review on hydrogen production and utilization: Challenges and opportunities. *Int. J. Hydrogen Energy* **2022**, *47*, 26238–26264. [CrossRef]
8. Liponi, A.; Pasini, G.; Baccioli, A.; Ferrari, L. Hydrogen from renewables: Is it always green? The Italian scenario. *Energy Convers. Manag.* **2023**, *276*, 116525. [CrossRef]
9. Suer, J.; Traverso, M.; Jäger, N. Carbon Footprint Assessment of Hydrogen and Steel. *Energies* **2022**, *15*, 9468. [CrossRef]
10. Yu, Z.Y.; Duan, Y.; Feng, X.Y.; Yu, X.; Gao, M.R.; Yu, S.H. Clean and Affordable Hydrogen Fuel from Alkaline Water Splitting: Past, Recent Progress, and Future Prospects. *Adv. Mater.* **2021**, *33*, 2007100. [CrossRef]
11. Zhou, K.L.; Wang, Z.; Han, C.B.; Ke, X.; Wang, C.; Jin, Y.; Zhang, Q.; Liu, J.; Wang, H.; Yan, H. Platinum single-atom catalyst coupled with transition metal/metal oxide heterostructure for accelerating alkaline hydrogen evolution reaction. *Nat. Commun.* **2021**, *12*, 3783. [CrossRef] [PubMed]
12. Zhang, H.; Zhou, W.; Lu, X.F.; Chen, T.; Lou, X.W.D. Implanting Isolated Ru Atoms into Edge-Rich Carbon Matrix for Efficient Electrocatalytic Hydrogen Evolution. *Adv. Energy Mater.* **2020**, *10*, 2000882. [CrossRef]
13. Liu, Z.; Qi, J.; Zeng, H.; Zeng, Y.; Wang, J.; Gu, L.; Hong, E.; Yang, M.; Fu, Q.; Chen, J.; et al. Electrochemical Preparation of Iridium Hydroxide Nanosheets with Ordered Honeycomb Structures for the Oxygen Evolution Reaction in Acid. *ACS Appl. Energy Mater.* **2022**, *5*, 6869–6877. [CrossRef]
14. Hu, M.; Ming, M.; Xu, C.; Wang, Y.; Zhang, Y.; Gao, D.; Bi, J.; Fan, G. Towards High-Efficiency Hydrogen Production through in situ Formation of Well-Dispersed Rhodium Nanoclusters. *ChemSusChem* **2018**, *11*, 3253–3258. [CrossRef] [PubMed]
15. Liu, H.; Wang, C.; Liu, C.; Zong, X.; Wang, Y.; Hu, Z.; Zhang, Z. Palladium nanoparticles confined in uncoordinated amine groups of metal-organic frameworks as efficient hydrogen evolution electrocatalysts. *Dalton Trans.* **2023**, *52*, 9705–9713. [CrossRef] [PubMed]
16. Subbaraman, R.; Tripkovic, D.; Strmcnik, D.; Chang, K.; Uchimura, M.; Paulikas, A.P.; Stamenkovic, V.; Markovic, N.M. Enhancing Hydrogen Evolution Activity in Water Splitting by Tailoring Li⁺-Ni(OH)₂-Pt Interfaces. *Science* **2011**, *334*, 1256–1260. [CrossRef]
17. Abdelghafar, F.; Xu, X.M.; Jiang, S.P.; Shao, Z.P. Designing single-atom catalysts toward improved alkaline hydrogen evolution reaction. *Mater. Rep. Energy* **2022**, *2*, 100144. [CrossRef]
18. Li, Q.; Chen, B.; Huang, L.; Zhu, S.; Qian, Y.; Wu, D.; Luo, S.; Xie, A. S-doped Ni(Fe)OOH bifunctional electrocatalysts for overall water splitting. *Int. J. Hydrogen Energy* **2024**, *51*, 1392–1406. [CrossRef]
19. Li, Y.; Li, H.; Li, Y.; Peng, S.; Hu, Y.H. Fe-B alloy coupled with Fe clusters as an efficient cocatalyst for photocatalytic hydrogen evolution. *Chem. Eng. J.* **2018**, *344*, 506–513. [CrossRef]

20. Nivetha, R.; Kollu, P.; Chandar, K.; Pitchaimuthu, S.; Jeong, S.K.; Grace, A.N. Role of MIL-53(Fe)/hydrated-dehydrated MOF catalyst for electrochemical hydrogen evolution reaction (HER) in alkaline medium and photocatalysis. *RSC Adv.* **2019**, *9*, 3215–3223. [[CrossRef](#)]
21. Wang, H.; Niu, C.; Liu, W.; Tao, S. d-Electron tuned CoMoP for enhance 5-hydroxymethylfurfural oxidation and HER. *Appl. Catal. B Environ.* **2024**, *340*, 123249. [[CrossRef](#)]
22. Diao, J.; Wang, S.; Yang, Z.; Qiu, Y.; Xu, R.; Wang, W.; Chen, K.; Li, X.; Chao, T.; Guo, X.; et al. Interfacial Electron Distribution of Co Nanoparticles Supported on N-Doped Mesoporous Hollow Carbon Spheres Endows Highly Efficient ORR, OER, and HER. *Adv. Mater. Interfaces* **2023**, *10*, 2202394. [[CrossRef](#)]
23. Bai, J.; Wang, Y.; Wang, Y.; Zhang, T.; Dong, G.; Geng, D. Self-reconstruction-induced c-CoSe₂ coupled with co(OH)₂ from Co_{0.85}Se For efficient HER Electrocatalysis in alkaline media. *Int. J. Energy Res.* **2022**, *46*, 12476–12484. [[CrossRef](#)]
24. Moroto, K.; Miyake, K.; Shu, Y.; Toyama, Y.; Ma, J.; Tanaka, S.; Nishiyama, N.; Fukuhara, C.; Kong, C.Y. Fabrication of NiS_x/C with a tuned S/Ni molar ratio using Ni²⁺ ions and Amberlyst for hydrogen evolution reaction (HER). *Int. J. Hydrogen Energy* **2020**, *45*, 24567–24572. [[CrossRef](#)]
25. Liu, Y.; Wang, J.; Tian, Q.; Liu, M.; Wang, X.; Li, P.; Li, W.; Cai, N.; Chen, W.; Yu, F. Papillae-like morphology of Ni/Ni(OH)₂ hybrid crystals by stepwise electrodeposition for synergistically improved HER. *Crystengcomm* **2019**, *21*, 3431–3438. [[CrossRef](#)]
26. Lai, W.; Ge, L.; Li, H.; Deng, Y.; Xu, B.; Ouyang, B.; Kan, E. In situ Raman spectroscopic study towards the growth and excellent HER catalysis of Ni/Ni(OH)₂ heterostructure. *Int. J. Hydrogen Energy* **2021**, *46*, 26861–26872. [[CrossRef](#)]
27. Xu, X.M.; Pan, Y.L.; Zhong, Y.J.; Ge, L.; Jiang, S.P.; Shao, Z.P. From scheelite BaMoO₄ to perovskite BaMoO₃: Enhanced electrocatalysis toward the hydrogen evolution in alkaline media. *Compos. Part B Eng.* **2020**, *198*, 108214. [[CrossRef](#)]
28. Islam, M.F.; Ahsan, M.; Islam, M.N.; Hossain, M.I.; Bahadur, N.M.; Aziz, M.A.; Al-Humaidi, J.Y.; Rahman, M.M.; Maiyalagan, T.; Hasnat, M.A. Recent Advancements in Ascribing Several Platinum Free Electrocatalysts Pertinent to Hydrogen Evolution from Water Reduction. *Chem.-Asian J.* **2024**, e202400220. [[CrossRef](#)] [[PubMed](#)]
29. Oyshi, T.A.; Islam, M.T.; Al-Humaidi, J.Y.; Rahman, M.M.; Hasnat, M.A. Nanoarchitectonics for optimization of a Ti/Au-IrOx electrode for enhanced catalytic performance pertinent to hydrogen evolution reaction. *Int. J. Hydrogen Energy* **2024**, *64*, 1011–1020. [[CrossRef](#)]
30. Islam, M.N.; Hossain, M.M.; Maktedar, S.S.; Rahaman, M.; Rahman, M.A.; Hasnat, M.A. Ce-Doped TiO₂ Fabricated Glassy Carbon Electrode for Efficient Hydrogen Evolution Reaction in Acidic Medium. *Chem.-Asian J.* **2024**, e20230114. [[CrossRef](#)]
31. Zhang, H.; Diao, J.; Liu, Y.; Zhao, H.; Ng, B.K.Y.; Ding, Z.; Guo, Z.; Li, H.; Jia, J.; Yu, C.; et al. In-Situ-Grown Cu Dendrites Plasmonically Enhance Electrocatalytic Hydrogen Evolution on Facet-Engineered Cu₂O. *Adv. Mater.* **2023**, *35*, e2305742. [[CrossRef](#)] [[PubMed](#)]
32. Calvary, C.A.; Hietsoi, O.; Hofsommer, D.T.; Brun, H.C.; Costello, A.M.; Mashuta, M.S.; Guo, Z.; Li, H.; Jia, J.; Yu, C.; et al. Copper bis(thiosemicarbazone) Complexes with Pendent Polyamines: Effects of Proton Relays and Charged Moieties on Electrocatalytic HER. *Eur. J. Inorg. Chem.* **2021**, *2021*, 267–275. [[CrossRef](#)]
33. Zhang, Y.; Zhou, B.; Wei, Z.; Zhou, W.; Wang, D.; Tian, J.; Wang, T.; Zhao, S.; Liu, J.; Tao, L.; et al. Coupling Glucose-Assisted Cu(I)/Cu(II) Redox with Electrochemical Hydrogen Production. *Adv. Mater.* **2021**, *33*, e2104791. [[CrossRef](#)] [[PubMed](#)]
34. Islam, M.N.; Ahmed, J.; Faisal, M.; Algethami, J.S.; Aoki, K.; Nagao, Y.; Harraz, F.A.; Hasnat, M.A. Efficient Electrocatalytic Hydrogen Evolution Reaction on CuO Immobilized Stainless-Steel Electrode Prepared by the SILAR Method. *ChemistrySelect* **2023**, *8*, e202301077. [[CrossRef](#)]
35. Di Natale, C.; Gros, C.P.; Paolesse, R. Corroles at work: A small macrocycle for great applications. *Chem. Soc. Rev.* **2022**, *51*, 1277–1335. [[CrossRef](#)] [[PubMed](#)]
36. Joseph, M.; Haridas, S. Recent progresses in porphyrin assisted hydrogen evolution. *Int. J. Hydrogen Energy* **2020**, *45*, 11954–11975. [[CrossRef](#)]
37. Niu, Y.; Li, M.; Zhang, Q.; Zhu, W.; Mack, J.; Fomo, G.; Nyokong, T.; Liang, X. Halogen substituted A₂B type Co(III)triarylcorroles: Synthesis, electronic structure and two step modulation of electrocatalyzed hydrogen evolution reactions. *Dye. Pigm.* **2017**, *142*, 416–428. [[CrossRef](#)]
38. Mahammed, A.; Mondal, B.; Rana, A.; Dey, A.; Gross, Z. The cobalt corrole catalyzed hydrogen evolution reaction: Surprising electronic effects and characterization of key reaction intermediates. *Chem. Commun.* **2014**, *50*, 2725–2727. [[CrossRef](#)] [[PubMed](#)]
39. Hao, J.X.; Liu, Z.; Xu, S.; Si, L.; Wang, L.; Liu, H. Electrocatalytic hydrogen evolution by cobalt(III) triphenyl corrole bearing different number of trifluoromethyl groups. *Inorganica Chim. Acta* **2024**, *564*, 121967. [[CrossRef](#)]
40. Sudhakar, K.; Mahammed, A.; Fridman, N.; Gross, Z. Trifluoromethylation for affecting the structural, electronic and redox properties of cobalt corroles. *Dalton Trans. Int. J. Inorg. Chem.* **2019**, *48*, 4798–4810. [[CrossRef](#)]
41. Yang, G.; Ullah, Z.; Yang, W.; Wook Kwon, H.; Liang, Z.X.; Zhan, X.; Yuan, G.Q.; Liu, H.Y. Substituent Effect on Ligand-Centered Electrocatalytic Hydrogen Evolution of Phosphorus Corroles. *ChemSusChem* **2023**, *16*, e202300211. [[CrossRef](#)] [[PubMed](#)]
42. Wan, B.; Cheng, F.; Lan, J.; Zhao, Y.; Yang, G.; Sun, Y.; Si, L.-P.; Liu, H.-Y. Electrocatalytic hydrogen evolution of manganese corrole. *Int. J. Hydrogen Energy* **2023**, *48*, 5506–5517. [[CrossRef](#)]
43. Liu, Z.Y.; Lai, J.; Yang, G.; Ren, B.P.; Lv, Z.; Si, L.; Zhang, H.; Liu, H.-Y. Electrocatalytic hydrogen production by CN-substituted cobalt triaryl corroles. *Catal. Sci. Technol.* **2022**, *12*, 5125–5135. [[CrossRef](#)]
44. Ren, B.P.; Yang, G.; Lv, Z.Y.; Liu, Z.; Zhang, H.; Si, L.; Liu, H.-Y. First application of Sn (IV) corrole as electrocatalyst in hydrogen evolution reaction. *Inorg. Chem. Commun.* **2023**, *152*, 110663. [[CrossRef](#)]

45. Lv, Z.Y.; Yang, G.; Ren, B.P.; Liu, Z.Y.; Zhang, H.; Si, L.P.; Liu, H.-Y.; Chang, C.-K. Electrocatalytic Hydrogen Evolution of the Cobalt Triaryl Corroles Bearing Hydroxyl Groups. *Eur. J. Inorg. Chem.* **2023**, *26*, e202200755. [[CrossRef](#)]
46. Chen, H.; Huang, D.; Hossain, M.S.; Luo, G.; Liu, H. Electrocatalytic activity of cobalt tris(4-nitrophenyl)corrole for hydrogen evolution from water. *J. Coord. Chem.* **2019**, *72*, 2791–2803. [[CrossRef](#)]
47. Lei, H.; Fang, H.; Han, Y.; Lai, W.; Fu, X.; Cao, R. Reactivity and Mechanism Studies of Hydrogen Evolution Catalyzed by Copper Corroles. *ACS Catal.* **2015**, *5*, 4978–5646. [[CrossRef](#)]
48. Feizi, H.; Bagheri, R.; Song, Z.; Shen, J.; Allakhverdiev, S.I.; Najafpour, M.M. Cobalt/Cobalt Oxide Surface for Water Oxidation. *ACS Sustain. Chem. Eng.* **2019**, *7*, 6093–6105. [[CrossRef](#)]
49. Jiang, Y.; Yang, C.; Yu, Y.; Zhou, Y.; Shang, Z.; Zhang, S.; Liu, P.; Zhu, J.; Jiang, M. Aromatic polyaroxydiazole pseudocapacitive anode materials with tunable electrochemical performance through side group engineering. *J. Mater. Chem. Mater.* **2023**, *12*, 364–374. [[CrossRef](#)]
50. Lei, H.; Liu, C.; Wang, Z.; Zhang, Z.; Zhang, M.; Chang, X.; Zhang, W.; Cao, R. Noncovalent Immobilization of a Pyrene-Modified Cobalt Corrole on Carbon Supports for Enhanced Electrocatalytic Oxygen Reduction and Oxygen Evolution in Aqueous Solutions. *ACS Catal.* **2016**, *6*, 6429–6437. [[CrossRef](#)]
51. Lin, H.; Hossain, M.S.; Zhan, S.; Liu, H.; Si, L. Electrocatalytic hydrogen evolution using triaryl corrole cobalt complex. *Appl. Organomet. Chem.* **2020**, *34*, e5583. [[CrossRef](#)]
52. Ahmad, E.; Rai, S.; Padhi, S.K. Proton reduction by a Ni(II) catalyst and foot-of-the wave analysis for H₂ evolution. *Int. J. Hydrogen Energy* **2019**, *44*, 16467–16477. [[CrossRef](#)]
53. Felton, G.A.N.; Glass, R.S.; Lichtenberger, D.L.; Evans, D.H. Iron-Only Hydrogenase Mimics. Thermodynamic Aspects of the Use of Electrochemistry to Evaluate Catalytic Efficiency for Hydrogen Generation. *Inorg. Chem.* **2006**, *45*, 9181–9184. [[CrossRef](#)] [[PubMed](#)]
54. Fang, J.; Lan, J.; Yang, G.; Yuan, G.; Liu, H.; Si, L. Synthesis of cobalt A₂B triaryl corroles bearing aldehyde and amide pyridyl groups and their performance in electrocatalytic hydrogen evolution. *New J. Chem.* **2021**, *45*, 5127–5136. [[CrossRef](#)]
55. Yan, Q.W.; Wu, L.W.; Liu, Z.; Chen, F.; Ling, C.; Liu, H.Y.; Xiao, X.-Y.; Si, L.-P. First application of antimony(III) corrole for electrocatalytic hydrogen evolution. *Green. Chem.* **2024**, *26*, 4574–4581. [[CrossRef](#)]
56. Peng, W.Y.; Lan, J.; Zhu, Z.M.; Si, L.P.; Zhang, H.; Zhan, S.Z.; Liu, H.Y. Synthesis of metal (Ga, Co and Fe) 5,15-bis(pentafluorophenyl)-10-ethoxycarbonylcorrole and their electrocatalytic hydrogen evolution activity. *Inorg. Chem. Commun.* **2022**, *140*, 109453. [[CrossRef](#)]
57. Xu, S.Y.; Cen, J.H.; Yang, G.; Si, L.P.; Xiao, X.Y.; Liu, H.Y. Electrocatalytic Hydrogen Evolution by Binuclear Metal (M=Co, Fe, Mn) Xanthine Bridged Bis-corrole. *Chem. Res. Chin. Univ.* **2024**. [[CrossRef](#)]
58. Lei, J.; Luo, S.; Zhan, S. A cobalt complex, a highly efficient catalyst for electro- and photochemical driven hydrogen generation in purely aqueous media. *Polyhedron* **2018**, *154*, 295–301. [[CrossRef](#)]
59. Wu, L.-W.; Yao, Y.-F.; Xu, S.-Y.; Cao, X.-Y.; Ren, Y.-W.; Si, L.-P.; Liu, H.-Y. Electrocatalytic Hydrogen Evolution of Transition Metal (Fe, Co and Cu)-Corrole Complexes Bearing an Imidazole Group. *Catalysts* **2024**, *14*, 5. [[CrossRef](#)]
60. Xu, X.; Zhao, Y.; Yang, G.; Si, L.P.; Zhang, H.; Liu, H.Y. Electrocatalytic hydrogen evolution of a cobalt A₂B triaryl corrole complex containing -N=PPh₃ group. *Int. J. Hydrogen Energy* **2022**, *47*, 19062–19072. [[CrossRef](#)]
61. Gagne, R.R.; Koval, C.A.; Lisensky, G.C. Ferrocene as an internal standard for electrochemical measurements. *Inorg. Chem.* **1980**, *19*, 2854–2855. [[CrossRef](#)]

Disclaimer/Publisher's Note: The statements, opinions and data contained in all publications are solely those of the individual author(s) and contributor(s) and not of MDPI and/or the editor(s). MDPI and/or the editor(s) disclaim responsibility for any injury to people or property resulting from any ideas, methods, instructions or products referred to in the content.